IVYSPRING INTERNATIONAL PUBLISHER

Theranostics

2017; 7(16): 3901-3914. doi: 10.7150/thno.20190

Research Paper

"One-Pot" Fabrication of Highly Versatile and Biocompatible Poly(vinyl alcohol)-porphyrin-based Nanotheranostics

Yan Luo[1, 2*], Hao Wu[2*], Caihong Feng[5], Kai Xiao[7], Xixiao Yang[6], Qiangqiang Liu[7], Tzu-yin Lin[3], Hongyong Zhang[3], Jeffrey H. Walton[2, 4], Yousif Ajena[2], Yide Hu[8], Kit S. Lam[2, 3]✉ & Yuanpei Li[2]✉

1. Department of Oncology, 153 Central Hospital, Zhengzhou 450042, PR China;
2. Department of Biochemistry and Molecular Medicine, UC Davis Comprehensive Cancer Center, University of California Davis, Sacramento, CA 95817, USA;
3. Department of Internal Medicine, Division of Hematology/Oncology, University of California Davis, Sacramento, CA 95817, USA;
4. UC Davis NMR Facility, Davis, CA 95616, USA;
5. Beijing Institute of Technology, Beijing, 100081, PR China;
6. Department of Pharmacy, Nanfang Hospital, Southern Medical University, Guangzhou 510515, PR China;
7. National Chengdu Center for Safety Evaluation of Drugs, West China Hospital, Sichuan University, Chengdu, 610041, PR China;
8. Department of Oncology, Second Affiliated Hospital, Third Military Medical University, Chongqing, 400037, PR China.

* Yan Luo and Hao Wu contributed equally to this study.

✉ Corresponding authors: Kit S. Lam MD, PhD, University of California Davis, 2700 Stockton Blvd, Sacramento, CA, 95817, Phone: 916-734-0910, Email: kslam@ucdavis.edu. Yuanpei Li, PhD, University of California Davis, 2700 Stockton Blvd, Sacramento, CA, 95817, Phone: 916-734-4420, Email: lypli@ucdavis.edu.

Received: 2017.03.21; Accepted: 2017.07.07; Published: 2017.09.05

Abstract

Nanoparticle-based theranostic agents have emerged as a new paradigm in nanomedicine field for integration of multimodal imaging and therapeutic functions within a single platform. However, the clinical translation of these agents is severely limited by the complexity of fabrication, long-term toxicity of the materials, and unfavorable biodistributions. Here we report an extremely simple and robust approach to develop highly versatile and biocompatible theranostic poly(vinyl alcohol)-porphyrin nanoparticles (PPNs). Through a "one-pot" fabrication process, including the chelation of metal ions and encapsulation of hydrophobic drugs, monodispersenanoparticle could be formed by self-assembly of a very simple and biocompatible building block (poly(vinyl alcohol)-porphyrin conjugate). Using this approach, we could conveniently produce multifunctional PPNs that integrate optical imaging, positron emission tomography (PET), photodynamic therapy (PDT), photothermal therapy (PTT) and drug delivery functions in one formulation. PPNs exhibited unique architecture-dependent fluorescence self-quenching, as well as photodynamic- and photothermal- properties. Near-infrared fluorescence could be amplified upon PPN dissociation, providing feasibility of low-background fluorescence imaging. Doxorubicin (DOX)-loaded PPNs achieved 53 times longer half-life in blood circulation than free DOX. Upon irradiation by near infrared light at a single excitation wavelength, PPNs could be activated to release reactive oxygen species, heat and drugs simultaneously at the tumor sites in mice bearing tumor xenograft, resulting in complete eradication of tumors. Due to their organic compositions, PPNs showed no obvious cytotoxicity in mice via intravenous administration during therapeutic studies. This highly versatile and multifunctional PPN theranostic nanoplatform showed great potential for the integration of multimodal imaging and therapeutic functions towards personalized nanomedicine against cancers.

Key words: poly(vinyl alcohol)-porphyrin; "one-pot" fabrication; theranostics; imaging; multimodal therapy.

Introduction

The development of multifunctional nanoparticles as **thera**peutic and diag**nostic** (theranostic) agents has great impact in cancer management [1-12]. It offers several promising applications including the non-invasive monitoring of drug pharmacokinetics, distribution and accumulation at target sites, assessment of the therapeutic outcomes and adjustment of the individualized treatment in real time [3, 7-10, 13-17]. These functions are particularly important for cancer treatment and could potentially improve the overall survival of cancer patients [18].

Theranostic nanoparticles could be produced by either inorganic or organic materials [19-21]. A variety of inorganic nanoparticles including semiconductor quantum dots [22], iron oxide nanoparticles [23-26], gold-based nanomaterials (nanocages [27, 28], nanoshells [29], nanorods [30] and hollow gold nanosphere [31, 32]) and carbon nanomaterials (carbon nanotube [33] and graphene [34]) that typically possess intrinsic fluorescent, magnetic, photothermal or other interesting physical properties, have the potential to be developed as multimodal imaging and therapeutic agents [35, 36]. However, those inorganic nanomaterials are generally non-biodegradable and their potential long-term *in vivo* toxicity must be taken into consideration prior to clinical development [37-42]. Another appealing system for theranostic applications is the biodegradable organic nanoparticles, such as liposomes and micelles. These nanoparticles are typically fabricated from the self-assembly of amphiphilic molecules [43-47]. Due to their robust biocompatibility and excellent drug loading capacity, organic nanoparticles have shown promising applications in clinic. There are increasing numbers of research reports, clinical trials and approved nanodrugs based on organic nanoparticles [48-50]. However, most of the organic nanoparticles are more likely used as drug carriers, instead of integrating multiple functionalities. Therefore, organic theranostic agents are less well-developed when compared to the inorganic type. Although several novel multifunctional nanoparticles [47, 51-58] based on micelles, liposomes, biodegradable polymers and conductive polymers have been explored for theranostic applications, for both pre-clinical and clinical settings [50, 59], there is plenty of room for development of organic-based multifunctional nanoparticles as theranostic agents.

Despite significant accomplishments in applications of nanotheranostic agents in pre-clinical settings [60-62], such as functional imaging and drug delivery, barriers remain for successful implementation of these agents in a clinical setting. Many of these translational barriers relate to the complexity of fabrication, batch-to-batch reproducibility and availability of large-scale production [63]. A simple yet effective approach to fabricate multifunctional nanotheranostic agents is urgently needed. In the present study, we report a new generation of multifunctional poly(vinyl alcohol)(PVA)-porphyrin-based nanoparticles (PPNs) using an extremely simple and cost-effective "one-pot" fabrication approach. By introducing drugs and imaging agents in the self-assembly procedure for PVA-porphyrin conjugates, we could reliably produce PPNs with a micellar structure, integrating multiple imaging and therapeutic modalities, including near-infrared (NIR) optical imaging, positron emission tomography (PET), and compound therapy [64, 65], such as photodynamic therapy (PDT) and photothermal therapy (PTT) [66-68], in one single nanoplatform. This research utilized simplest materials and approach to achieve the most diverse and efficient theranostic functionalities. To the best of our knowledge, this is the first example of nanoparticle based on PVA that has achieved such broad applications.

Materials & Methods

Synthesis of PVA-porphyrin conjugates

The PVA-porphyrin conjugates were conveniently prepared by conjugating PVA (molecular weight: 27KDa) with different level of porphyrin derivatives through ester formation [64]. Briefly, the solution of PVA in DMSO was added to a solution of pyropheophorbide a, N,N'-dicyclohexylcarbodiimide (DCC), 4-(dimethylamino)-pyridine (DMAP), and N-hydroxybenzotriazole (HOBT) in DMSO. The reaction was kept under room temperature for 48 hrs. 5 times volume of cold ethanol was then added into the reaction mixture to precipitate PVA-porphyrin conjugates after reaction; the polymer was further washed with ethanol for 3 times and then dissolved in DMSO followed by dialysis against distilled water for 48 hrs. Finally, the PVA-porphyrin conjugates were lyophilized. The amount of conjugated porphyrin on PVA was quantified by the measurement of absorbance at 680 nm by ultraviolet-visible spectroscopy. The PVA-porphyrin conjugates were analyzed by 600 MHz Avance III NMR Spectrometer (Bruker, German) and fourier transform infrared spectroscopy (FTIR). Pyrene ratiometric method was employed to determine the critical micelle concentrations (CMC) value of the PVA-porphyrin. Briefly, 999 μL of

different concentrations of PVA-porphyrin were prepared, and 1 μL of 0.1 mM pyrene solution (in acetone) was introduced into the PVA-porphyrin solutions and yielded 0.1 μM pyrene solution. The PVA-porphyrin and pyrene contained solutions were then transferred into a 96-well plate and incubated at 37 °C for 2 h. After the incubation, the fluorescence of each well was evaluated by a microplate reader (excitation is 335 nm). The I_3/I_1 values were recorded for CMC assessment.

Preparation and characterization of doxorubicin-loaded PVA-porphyrin

Hydrophobic drugs such as DOX could be loaded into PPNs during the self-assembly of PVA-porphyrin conjugates via dialysis method. DOX was loaded into PVA-porphyrin nanoparticles (PPNs) by dialysis of a polymer/DOX solution in DMSO against PBS buffer. DOX and PVA-porphyrin (1mg/20mg) was first dissolved in DMSO, and then the solution was adjusted pH 8.5 with borate buffer, followed by dialysis against PBS for 3 hours. Free DOX was removed via column filtration with a 10 kDa molecular weight cut off membrane. The amount of encapsulated DOX was determined using absorbance measurement by diluting PPNs-DOX solution 10 times in DMSO. The calibration curve was obtained using a series of DOX/DMSO standard solutions with different concentrations. The morphology and particle size distribution of PPNs-DOX nanoparticles were characterized by transmission electron microscopy (TEM, Philips CM-120) and dynamic light scattering (DLS, Microtrac), respectively. *In vitro* drug release profiles were carried out using the dialysis method. Aliquots of DOX-loaded PPNs solution were injected into a dialysis cartridge with a molecular weight cutoff of 3.5 kDa. The whole dialysis process was carried out at 37°C with gentle rocking on a rotating platform (at 70 rpm) in the presence of 10 g/L activated charcoal in 1L PBS. The concentration of DOX remained inside the dialysis cartridge at various time points was determined by absorbance measurement.

Preparation of metal-chelated PPNs

Metal ions, such as Cu^{2+} could be loaded via chelation during or after drug loading. The $^{64}Cu^{2+}$ chelation was carried out through the addition of $^{64}CuCl_2$ (Washington University, MO, USA) to the PVA-porphyrin aqueous solution under stirring for 2 hrs at room temperature [47, 69]. The free metal ions in the PPNs solution were removed via column filtration using Micro Bio-Spin 6 columns (Bio-Rad, Hercules, CA, USA). Instant thin-layer chromatography (ITLC) was immediately performed to evaluate the radiochemical purity and yield after the incorporation of ^{64}Cu into the PPNs.

Cellular uptake and *In vitro* cytotoxicity studies

The uptake profiles of DOX-loaded PPNs in SKOV-3 ovarian cancer cells were qualitatively observed by confocal microscopy. SKOV-3 cells were seeded in an 8-well slide. When the cells were 80%~90% confluent, cells were incubated with free DOX and PPNs-DOX (final concentration of DOX = 86 μM) for 30min and 6 hrs at 37 °C with 5% CO_2, respectively. Then the cells were washed thrice with PBS buffer, fixed with 4% paraformaldehyde for 15 min. The nuclei were stained with DAPI. The slides were mounted with coverslips and observed under a confocal microscope.

MTS assay was carried out to evaluate the *in vitro* cytotoxicity of free DOX, empty PPNs and PPNs-DOX against ovarian cancer cells. SKOV-3 cells were seeded in 96-well plates at the cell densities of 0.5×10^4 cells/well, respectively. After 24 hrs incubation, cells were treated with different concentrations of free DOX, PPNs-DOX, and equivalent doses of empty PPNs. At 72 hrs, MTS was added to each well and further incubated for another 2 hrs. The absorbance at 490 nm was detected with a microplate reader. The photosensitizing function of PPNs was evaluated as well. The cells were incubated with empty PPNs and PPNs-DOX, respectively. After 6 hours treatment, cells were washed with PBS 3 times, and replaced with fresh medium in the plates followed by exposure to 30 mW/cm² NIR light for 2 min. At 72 hrs after light irradiation, cell viability was determined using MTS assay. To measure intracellular ROS production in ovarian cancer cells, the cells were incubated in medium containing 10 μM 2′,7′-Dichlorofluorescin diacetate (DCF) for 30 min after light irradiation. The cells were washed thrice with PBS and fluorescent images were immediately acquired under fluorescence microscope using Metamorph programme. Other cells were trypsinized and used for flow cytometry analysis. Then mitochondrial membrane potential ($\Delta\Psi m$) was evaluated in pre-treated ovarian cancer cells with PPNs. At 18 hrs after illumination with NIR light, cells were loaded with 50nM DiOC6(3) for 20 min. At the same time, cells were stained with propridium iodide (dead cells) and Hoechst 33342 (nucleus). Fluorescent images were acquired using fluoresce microscope. In order to further investigate the cellular response to PPNs and photodynamic therapy, SKOV-3 cells were treated with or without 10μM PPNs for 2 hrs followed by exposure with or without light for 2 min. After 24 or 48 hrs incubation, expression level of cleaved caspase3 was measured by western blot. Lastly, cell

morphology was studied via Hema3® staining. SKOV-3 cells were seeded on 6-well plate, treated with or without 10μM PPNs for 2 hrs. 16 hrs after light irradiation, cells were stained with Hema3®, observed under fluorescence microscopy.

NIRF optical imaging

All animal experiments present in this study were performed according to animal protocols approved by the Animal Care and Use Administrative Advisory Committee at University of California, Davis. Female nude mice ages 6 to 8 weeks were purchased from Harlan Laboratories. Ovarian cancer xenograft mouse model was established by subcutaneously injecting 5×10^6 SKOV-3 cells resuspended in 100 μl of mixture of PBS and Matrigel (1:1, v/v) at the right flank. When tumor xenograft reached 6 to 10 mm in diameter, the mice were subjected to NIRF optical imaging. For each mouse, 200 μl PBS solution of PPNs (20mg/mL) was injected via tail vein (n=5). At different time points (0.15, 3, 6, 24, 48 and 82 hrs) post-injection, mice were anesthetized by intraperitoneal injection of pentobarbital (60mg/kg), and scanned using Kodak multimodal imaging system IS2000MM with the excitation at 625 nm and the emission at 700 nm. At 6, 24, 48 and 82 hrs after *in vivo* imaging, mice were euthanized. Tumors and all major organs were excised for *ex vivo* imaging.

Pharmacokinetic studies

The jugular vein of male Sprague–Dawley rats was cannulated and a catheter was implanted for intravenous injection and blood collection (Harland, Indianapolis, IN, USA). Free DOX (5mg/kg) and PPNs-DOX (5mg/kg) were administrated into rats (n = 3) intravenously. At pre-determined time points, blood samples (~100 μl) were collected via jugular vein catheter. The kinetics of DOX were measured through testing the fluorescence of 590 nm (excitation is 485 nm). The values were plotted versus time after the subtraction of blood background.

PET imaging

Real-time bio-distribution of the injected ^{64}Cu-labeled PPNs [70-73] was evaluated by PET.Nude mice bearing SKOV3 ovarian cancer xenografts at pre-injection and 4, 8, 16, 24 and 48 hr post-injection of ^{64}Cu-labelled PPNs (100 μl, ^{64}Cu dose: 0.5 mCi) were scanned on a microPET system (Siemens Inveon D-PET) using standard imaging protocols for pharmacokinetic studies developed in the UCD Cancer Center Animal Imaging Shared Resource [74].

Photodynamic/photothermal laser irradiation

The thermal effect during irradiation was evaluated by monitoring the temperature of PPNs solutions using an infrared thermal camera (FLIR). PVA-porphyrin solutions in the absence and in the presence of SDS were irradiated with a 690 nm diode laser system (Applied Optronics, Newport, CT), and the power was measured as 1 W with a spot size of 5 mm diameter for 30 s. The concentrations of PPNs in the solutions were 0.019 to 0.3 mg/mL, calculated on porphyrin content. The tumor temperature in SKOV-3 bearing mice was also monitored during irradiation. PPNs were injected via tail vein into the mice at a dose of 2 mg/kg based on the porphyrin content. After 24 hrs, the tumor was irradiated with a 690 nm laser at a light dose of 1.25 W/cm^2 for 180 s. Tumor temperature changes in PBS control mice were also recorded with the thermal camera. After light irradiation, the tumor was immediately harvested to measure intratumoral ROS production. DCF was used as the ROS indicator by mixing with 100 μL of tissue lysates derived from tumors treated with PPNs and PBS. To evaluate PDT/PTT caused tumor ablation, the whole tumors were dissected 24 hours after irradiation. The specimen were fixed in 10% formaldehyde, cut into thin slices and stained with H&E. The sections were viewed and photographed under a bright-field microscopy at 20X.

Phototherapy and tumor response

Subcutaneous SKOV-3 tumor-bearing mice were used for *in vivo* therapeutic study when tumor volumes reached 80-120 mm^3 (designate as Day 0). The therapeutic efficacy and toxicity profiles of different PPNs formulations were evaluated. On day 0, all mice were randomly divided into seven groups (n=6). Mice were intravenously administered with PBS, empty PPNs, DOX·HCl and PPNs-DOX. The DOX was given at the dose of 2.5mg/kg, and PPNs was given at the dose of 2 mg/kg, calculated based on the porphyrin content. The treatment was given every 5 days on day 0, 5, 10 and 15 for a total 4 doses. For the PPNs group, mice were irradiated under anesthesia with a 690 nm laser at a light dose of 0.5 W/cm^2 or 1.25 W/cm^2 for 120 s 24 hrs after the injection, and the light dose for PPNs-DOX group was set at 0.5 W/cm^2 for 120 s. Tumor size and body weight were measured twice a week. Tumor volume was calculated using the equation $(L\times W^2)/2$, where L is the longest and W is shortest in tumor diameters (mm). For humane reasons, mice were sacrificed when tumor volume reached 1000 mm^3, which was considered as the end point of survival data. At day 5 after the last dosage, blood samples were collected from each group to test blood cell counts and serum chemistry.

Statistical analysis

Data were presented as mean ± standard error (SEM). Student's t-test was used to analyse the statistical differences between two groups, and one-way ANOVA for multiple groups. A value of $P < 0.05$ was considered as statistically significant.

Results

Preparation and characterization of PPNs

Fig.1A schematically illustrates the chemical structure of PVA-porphyrin conjugates (PVA-Por), and how they can be used to fabricate multifunctional nanoparticles via "one-pot" approach. PVA-Por was conveniently synthesized via the conjugation of pyropheophorbide a, a chlorophyll derived phorphyrin analogue [75], to the hydroxyl group of PVA via one-step ester formation. The amount of conjugated porphyrin on PVA was calculated according to the calibration curve between the absorbance at 680 nm and concentrations of porphyrin standard (Fig. S1). ^{1}HNMR spectra of PVA-Por (Fig. S2) revealedpeaks (9.80, 9.47 and 8.32 ppm) that are unique for pyropheophorbide a, and the absence of the peak characteristic for carboxylic acid. The 1703, 1101 and 1027 cm^{-1} peaks shown in the FTIR spectrum of PVA-Por (Fig. S3) confirmed the formation of ester linkage. PVA-Por can self-assemble to form PPNs in aqueous environment with a hydrophobic porphyrin core surrounded by hydrophilic PVA chains and a π- π stacking between DOX and porphyrin (Fig.1A). The morphology of PPNs was observed under a TEM. As shown in Fig.1B, PPNs in PBS exhibited spherical shapes and relatively uniform size distribution. At higher magnifications, a typical core-shell structure of PPNs was observed (Fig.1C). The particle size of PPNs in PBS was determined by DLS to be 78 nm in diameter, which was consistent with that observed by TEM (Fig.1D). The critical micelle concentration of PPNs was determined to be 0.040 μM (Fig. S4). PVA-Por exhibited two main absorption peaks, one at 405 nm and one in the near-infrared window at 680 nm (Fig.1F). As shown in Fig.1g, the NIR fluorescence of PPNs in PBS was quenched, likely due to the π-π interactions and hydrophobic characteristics of Por molecules [47]. In contrast, when using sodium dodecyl sulfate (SDS) to disrupt the PPNs, the NIR fluorescence at around 680 nm increased dramatically. Further, NIR fluorescence imaging also demonstrated tremendously higher fluorescence after dissociation of PPNs with the addition of SDS (Fig.1G).

Besides their unique photonic properties, the PPNs could efficiently encapsulate hydrophobic drugs such as doxorubicin (DOX) during the nanoparticle formation by the self-assembly of PVA-Por. Fluorescence quantum yield of PPNs was measured to be 12.6 % (Fig. S5). The loading efficiency (LE) for DOX approached 75% when the ratio of DOX to PPNs was 5% (w/w %). However, the LE decreased to 62% and 53%, when the initial amount of DOX increased to 10% and 20%, respectively. The highest DOX loading achieved was 10.6% (w/w %) in these studies and could be considered as the loading capacity of PPNs for DOX. The particle size changed to 34 nm when the initial DOX amount was 5%. It was slightly decreased compared to the empty PPNs without payload. This is likely due to the formation of tighter aggregation in the presence of hydrophobic drug, as suggested by other reports[76, 77]. With increasing amount of DOX loading, the particles size increased gradually and the particle size distribution was broadened (Fig.1H). The release profile of DOX from DOX-loaded PPNs (PPNs-DOX) was studied using a dialysis method [44]. As shown in Fig.1I, free DOX rapidly diffused out of the dialysis cartridge and 90% of free DOX was released within the first 5 hrs. In contrast, PPNs-DOX could release DOX in a sustained manner, with initial release of 11% of DOX during the first 5 hrs as shown in Fig.1I. Subsequently, PPNs-DOX showed a slow linear release profile and released 66% of drug in 72 hrs. The stability of PPNs-DOX was also evaluated. Both the particle size and drug content showed no significant changes over 3 months at 4 ^oC in PBS. Batch-to-batch reproducibility of PPNs was satisfactory with mean particle size maintained between 61 nm to 90 nm (Fig. S6), and PPNs-DOX was found to be stable in cell culture environment with 10% FBS over at least 10days (Fig. S7).

Cellular uptake and *in vivo* biodistribution study

Cellular uptake efficiency of PPNs in SKOV3 ovarian cancer cells was quantified with flow cytometry at different incubation time points (Fig.2A). The fluorescence intensity of PPNs was found to rapidly increase after 15 min incubation, and remained stable after 4 hrs. At 24 hrs, the fluorescence intensity of PPNs was up to 8.4 times higher than that in 15 min (Fig.2A). Intracellular uptake behavior and localization of free DOX and PPNs-DOX were examined in SKOV-3 cells with confocal microscopy (Fig.2B). After 30 min incubation, DOX fluorescence from PPNs-DOX was mainly located in the cytoplasm while that from free DOX could be observed in the nuclei. At 6 hrs after incubation, DOX fluorescence signal of the free DOX group was completely inside the nuclei, buta small amount of the DOX signal

remain in the cytoplasm. In contrast, the porphyrin fluorescence signal of the nanocarrier in the PPNs-DOX group was low at 30 min but remained high in the cytoplasm at 6 hrs (Fig.2B). *In vivo* pharmacokinetic study in rats showed that PPNs greatly prolonged the circulation time of DOX in the blood (Fig.2C & Fig. S8, S9). PPNs-DOX group exhibited a 5 times higher area under curve (AUC) and 53 times longer half-life of the terminal phase ($t_{1/2}$) than that of free DOX groups. The major side-effect of DOX is cardio-toxicity [78]. Interestingly, decreased cardiac accumulation of DOX was observed by using the formulation of PPNs-DOX compared to free DOX, indicating that PPNs may be able to reduce the cardio-toxicity of this drug (Fig. 2D).

Imaging capabilities of PPNs

As shown in Fig. 1G, PPNs emit NIR fluorescence with a peak at 680 nm, which is intrinsically suitable for *in vivo* fluorescence optical imaging. The real-time distribution, excretion, and tumor targeting efficiency of PPNs can be conveniently monitored after intravenous injection into mice bearing SKOV3 ovarian cancer xenografts. At 5 min after injection, there was strong overall fluorescence signal of the entire animal (Fig. S10). Subsequently, preferential PPNs accumulation at tumor sites was observed from 6 hrs to 82 hrs after administration, which is probably attributed to the enhanced permeability and retention (EPR) effect (Fig. 2E)[30]. Fluorescence intensity of the *in vivo* SKOV-3 tumor was found to peak at 18 hrs post-injection (Fig. S11). *Ex vivo* images (Fig. 2F) at different time points post-injection further confirmed the preferential uptake and retention of PPNs in tumor tissue, compared to other normal organs, although there was some uptake in liver and lung at 6 hrs, which is likely due to the nonspecific clearance by Kupffer cells and macrophages[30], respectively.

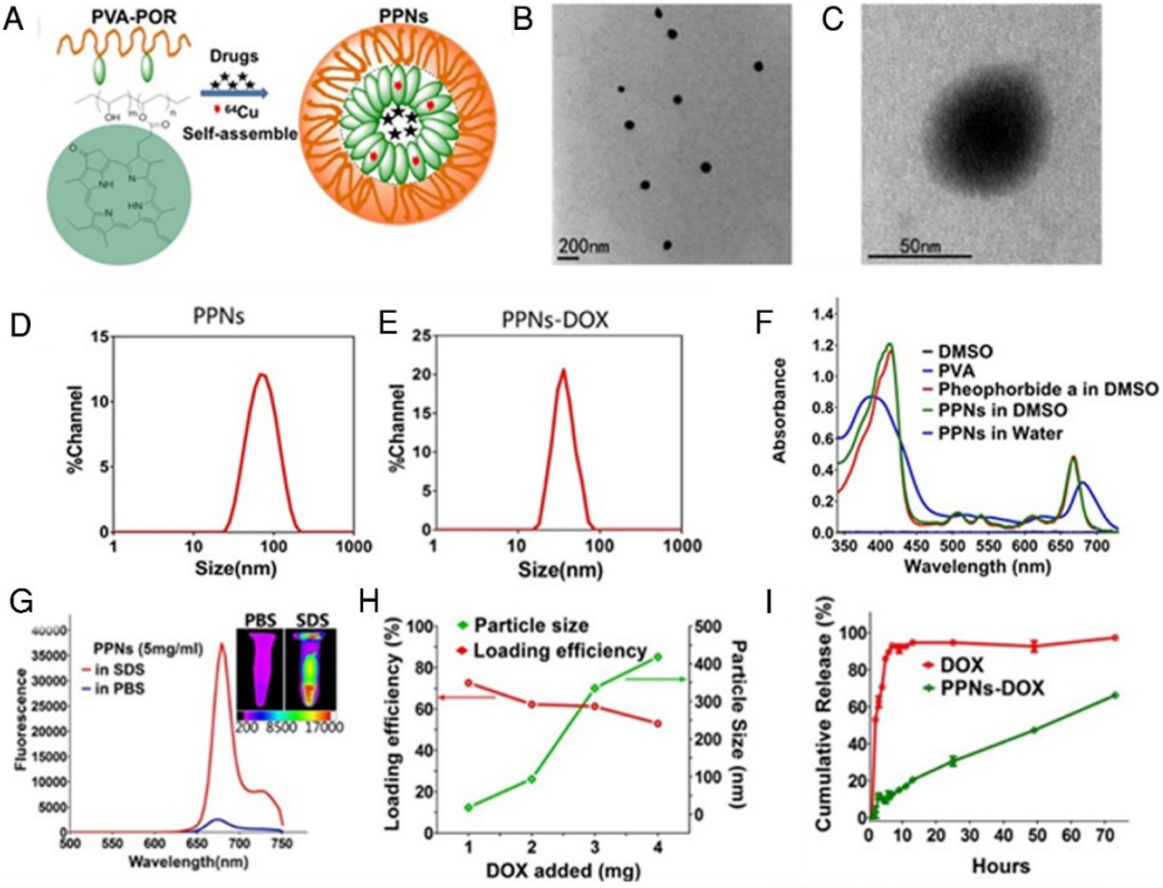

Figure 1. The schematic illustration of fabrication of PPNs by one-pot approach and characterizations of the resulting PPNs. (**A**) Schematic representation of PPNs prepared by the self-assembly of PVA-porphyrin conjugates. (**B, C**) TEM images of PPNs stained with phosphotungstic acid. (**D, E**) Size distribution of PPNs and DOX-loaded PPNs (PPNs-DOX, DOX initial loading at 1mg/20mg PPNs) in PBS, measured by dynamic light scattering (DLS). (**F**) Absorption spectra of PVA (blue), pyropheophorbide a (red) and PVA-porphyrin conjugates (green) in DMSO & water. (**G**) Fluorescence emission spectra of PPNs in PBS (blue) versus dissociated state of PPNs in the presence of SDS (red), as well as near-infrared imaging of PPNs solutions in PBS and SDS, respectively. (**H**) The DOX loading efficiency of PPNs and the particle size change of PPNs-DOX versus the level of drug added at initial loading. The amount of DOX was varied from 1 to 4 mg while that of PVA-porphyrin was kept at 20mg. PPNs-DOX with initial loading at 1mg/20mg PPNs were used for the following *in vitro* and *in vivo* studies. (**I**) Cumulative DOX release profiles from free DOX and DOX-loaded PPNs by dialysis method.

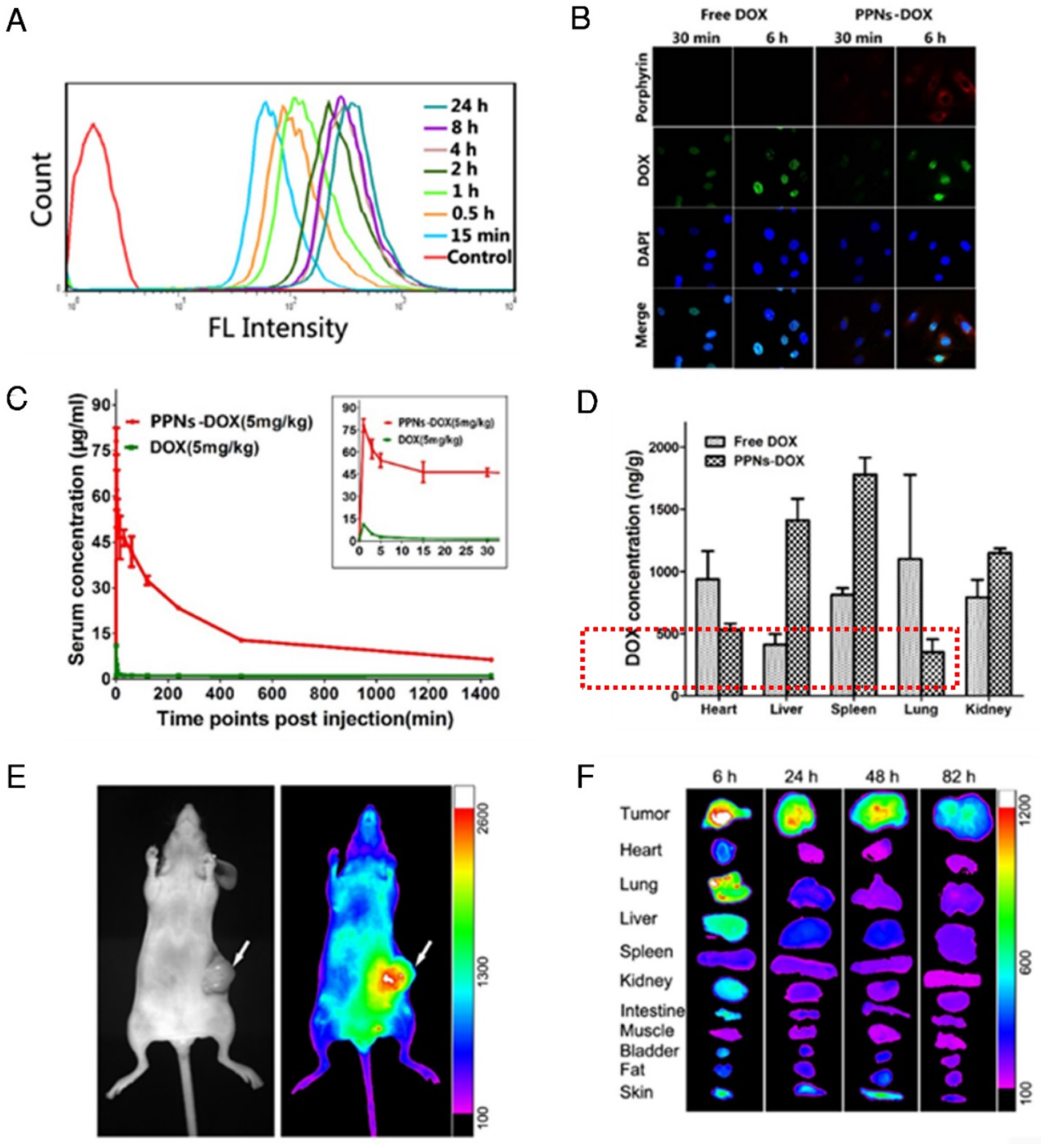

Figure 2. Cell uptake, *in vivo* and *ex vivo* near-infrared optical imaging of PPNs. (**A**) Porphyrin fluorescence in SKOV-3 cells after incubation with PPNs (0.1mg/mL) at different time points. (**B**) Confocal images of SKOV-3 cells incubated with 100 μg/ml free DOX and DOX-loaded PPNs for 30 min and 6 h. (**C**) Pharmacokinetic study of free DOX (5mg/kg) and PPNs-DOX (5mg/kg) in rats. (**D**) The biodistribution of free DOX (5mg/kg) and DOX from PPNs-DOX (5mg/kg) in rats. (**E**) Representative *in vivo* NIFR optical images (Por channel) of subcutaneous SKOV-3 tumor-bearing mice at 18 hrs after intravenous administration of PPNs (20mg/ml). (**F**) *Ex vivo* optical images (Por channel) of tumors and major organs of SKOV-3 xenograft-bearing mice euthanized at different time points post-injection of PPNs.

In addition to their unique photonic properties and excellent drug loading capacity, PPNs could conveniently chelate imaging agents such as copper ($^{64}Cu^{2+}$), because of porphyrins and its derived analogue with a tetrapyrrole skeleton that can chelate with an incredibly diverse range of metal ions to form metalloporphyrin complexes [79, 80]. The chelation could be done separately or simultaneously with the drug loading procedure through the self-assembly of PVA-Por. The free metal ions in the PPNs solution were removed via column filtration. Instant thin-layer chromatography (ITLC) was immediately performed to evaluate the radiochemical purity and yield after the incorporation of ^{64}Cu into the PPNs. After

centrifuge filtration, approximate 95% radiochemical purity was achieved, indicating that ^{64}Cu-labeled PPNs could be used as a potential positron emission tomography (PET) imaging probe [47, 81] (Fig. S12).

PET is a promising noninvasive imaging method to monitor the real-time bio-distribution of radionuclide-labeled nanoparticles and drugs in real time [70-73]. We applied PET to study the *in vivo* distribution of the injected ^{64}Cu-labeled PPNs. PET imaging (Transverse, Coronal and Sagittal) showed that ^{64}Cu-labelled PPNs started to accumulate at tumor sites 16 hrs after injection (Fig. S13). The ^{64}Cu signal at tumor site continued to increase over a period of 48 hrs (Fig. S13). It should be noted that the center of the tumor was necrotic, which may explain why radio-uptake was low at the center of the tumor.

In vitro antitumor efficacy

The *in vitro* antitumor efficacy of free DOX, empty PPNs and DOX-loaded PPNs against SKOV-3 ovarian cancer cells after 72 hrs continuous exposure were investigated by MTS assay. As shown in Fig.3A, similar dose-dependent cytotoxicity was observed for free DOX and PPNs-DOX. Additionally, the empty PPNs did not exhibit detectable cytotoxic effects at all the concentrations up to 20 mg/mL without light exposure. Furthermore, the phototoxic effect of PPNs against SKOV-3 cells was studied, by exposure of NIR light at 30 mW/cm^2 for 15 s, 30 s, 1 min, 2 min and 4 min, respectively. Prior to the light irradiation, the cells were incubated with different concentrations of PPNs for 2 hrs, followed by thoroughly washing and replacing the medium. The results of MTS assay demonstrated both a light-dose dependent and PPN-concentration dependent cell killing upon light illumination (Fig.3B). Interestingly, PPNs-DOX was able to take advantage of both chemotherapy and photodynamic therapy for cell killing. The combination therapy via PPNs-DOX was significantly more efficacious than free DOX, PPNs-DOX without light and PPNs mediated photodynamic therapy alone (Fig.3C). The mechanism of cell death after light irradiation was further investigated. Compared to the control group, significantly increased reactive oxygen spices (ROS) production was detected by flow cytometry (Fig.3D). Furthermore, obvious increased ROS fluorescence was observed under fluorescence microscopy (Fig. S14). The ROS production led to loss of mitochondrial membrane potential and cell apoptosis, verified by propidium iodide (PI) and 3,3'-Dihexyloxacarbocyanine Iodide ($DIOC_6(3)$) co-staining (Fig.3E) and increased cleaved caspase-3 activation (Fig.3F), respectively. As shown in Fig. 3E, cells in the control group displayed green fluorescence of $DIOC_6(3)$ without red fluorescence of PI, whereas cells in the treated group displayed only red fluorescence of PI, suggesting that the cells were killed upon light irradiation. The cellular damage was also observed after the light irradiation (Fig.3G).

PPNs mediated multimodal therapy

Not only do PPNs have imaging functions, they can also be used as photosensitizer for PDT and PTT. We have previously demonstrated that there was significant photothermal transduction (heat generation) associated with intact porphyrin-based nanoparticles while obvious photodynamic effect (ROS production) was found when the nanoparticles were dissociated [47]. The heat generation and photodynamic effect (ROS production) of PPNs was investigated *in vitro* and in tumors. Compared with PBS and small-molecule pyropheophorbide a, PPNs displayed a much higher photothermal conversion efficiency (Fig. S15). As PPNs are highly self-quenched in PBS (Fig. S16), the thermal effect of PPNs during different dose of light irradiation was evaluated using a thermal camera. The temperature increased rapidly from 31 ^{o}C to 54 ^{o}C when PPNs solutions at a concentration of 0 to 0.3 mg/mL porphyrin were exposed to 690 nm laser at 1.25 W/cm^2 for 30 s. When PPNs were dissociated in the presence of SDS, same dose of light caused a mild and continuous temperature increase to 42 ^{o}C. However, with a laser at 0.5 W/cm^2, the temperature of PPNs in PBS and PPNs in SDS only increased to 33 ^{o}C and 31 ^{o}C, respectively (Fig.4A). Meanwhile, PPNs were able to retain their structural stability upon multiple irradiations by 690 nm laser (Fig. S17). The efficiency of photothermal transduction of PPNs *in vivo* was further investigated by recording tumor temperature during irradiation compared to PBS controls (Fig.4B). The SKOV-3 xenograft-bearing mice were intravenously injected with 3 mg/kg PPNs or PBS. The tumors were then irradiated with 690 nm light at 1.25 W/cm^2 for 3 min at 24 hrs post-injection. The tumor temperature in the PBS control group increased moderately to 38 ^{o}C while that in PPNs group increased dramatically from 28 ^{o}C to 56 ^{o}C at the end of 3 min irradiation. However, with irradiation at 0.5 W/cm^2 for 3 min, a mild increase to a final temperature of 31 ^{o}C and 33 ^{o}C was observed in the PBS control group and PPNs group, respectively (Fig.4C, D). Moreover, the ROS production in the tumors upon laser irradiation was measured. In contrast to PBS control group, significantly higher ROS was generated by light irradiation in the PPNs group with irradiation at 0.5 W/cm^2 for 3 min (Fig.4E).

The antitumor efficacy of PPNs was further assessed by monitoring the growth rate of tumors in

an *in vivo* subcutaneous model bearing ovarian cancer xenograft (Fig.5A). Free DOX and PPNs-DOX at the equivalent dose of DOX (2.5 mg/kg), PPNs and PPNs-DOX at the equivalent dose of porphyrin (2 mg/kg), as well as the PBS control were intravenously administrated every five days on days 0, 5, 10 and 15 respectively. Interestingly, mice receiving 2.5 mg/kg free DOX did not exhibit obvious antitumor effect compared to the PBS control group, whereas mice receiving 2.5 mg/kg PPNs-DOX did slow down the tumor growth considerably. In another group, tumors treated with PPNs and laser irradiation (690 nm laser at 0.5 W/cm^2 for 2 min) showed similar decreased tumor growth rate. Furthermore, PPNs-DOX mediated combination of phototherapy (low dose, 0.5 W/cm^2 for 2 min) with same dose of DOX showed remarkable delay in tumor growth compared to PPNs-DOX without light or with 690 nm laser at 0.5 W/cm^2 for 2 min. Under irradiation with high dose of light at 1.25 W/cm^2 for 2 min, mice developed eschars on the tumors starting from day 2 post-treatment, and the tissue healed in the following 2 weeks. By day 45, the group of mice received high light dose (690 nm laser at 1.25 W/cm^2 for 2 min) achieved 100% survival rate; only one out of six mice in this group exhibited tumor recurrence. The survival rate of mice in all groups was presented by the Kaplan-Meier survival curves shown in Fig. 5B. For the mice treated with free DOX or laser-alone, no obvious prolonged survival rate was observed compared to the PBS control group. While mice in the PPNs-DOX treated group (no light) started to reach the end point on day 24, and all the mice were euthanized by day 36. However, the mice receiving combination therapy of phototherapy (low dose, low dose, 0.5 W/cm^2 for 2 min) with DOX achieved 80% survival rate by day 40, then the tumors recurred and 50% of the mice reached the end point by day 45. H&E staining of tumor tissue after phototherapy was performed to evaluate treatment efficacy (Fig.5C, D). In the control tumor, no necrosis or obvious cellular damage was noticed, whereas the tumor received low dose of light exhibited signs of sporadic necrosis. Furthermore, tumors irradiated with high dose of light showed extensive cell destruction and loss of tissue architecture.

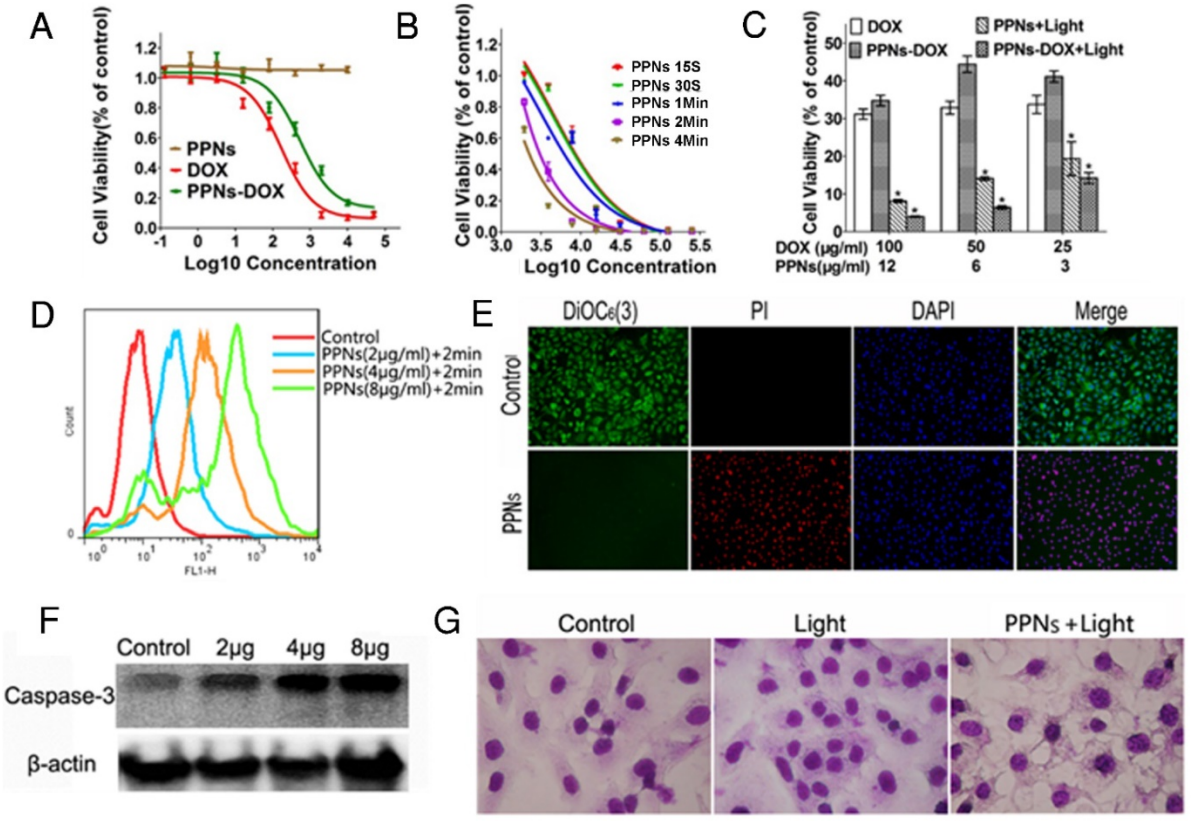

Figure 3. ***In vitro*** **antitumor effects of PPNs mediated chemotherapy and photodynamic therapy.** (**A**) Cytotoxicity of empty PPNs and the antitumor effects of PPNs-DOX in SKOV-3 ovarian cancer cells, compared with free DOX. (**B**) Cell viability of SKOV-3 cancer cells after 2 hrs incubation with PPNs followed by exposure of 30 mW/cm^2 NIR light for 15 s, 30 s, 1 min, 2 min and 4 min. (**C**) Cell killing effect of DOX combined with PPNs mediated photo-therapy. SKOV-3 cancer cells were treated with PPNs, free DOX, and PPNs-DOX for 6 hrs. Cells were irradiated with light for 2 min, and cell viability was measured by MTS assay after 72 hrs (P<0.05). (**D**) ROS production was quantified by flow cytometry in SKOV-3 cancer cells treated with different concentrations of PPNs for 2 hrs, followed by 30 mW/cm^2 laser irradiation for 2 min. (**E**) SKOV-3 cancer cells were incubated with 100 μg/mL PPNs for 2 hrs followed by light irradiation for 2 min. 24 hrs later, cells were stained with 40 nM $DiOC_6(3)$ (Green, mitochondrial membrane potential), propridium iodide (PI, red, dead cells) and Hoechst 33342 (blue, nucleus). (**F**) SKOV-3 cancer cells were treated with different concentrations of PPNs for 2 hrs followed by PDT. Cleaved caspase-3 expression was measured by western blot analysis 24 h later. (**G**) Cell morphology of SKOV-3 cancer cells after PDT was evaluated by Hema 3 staining.

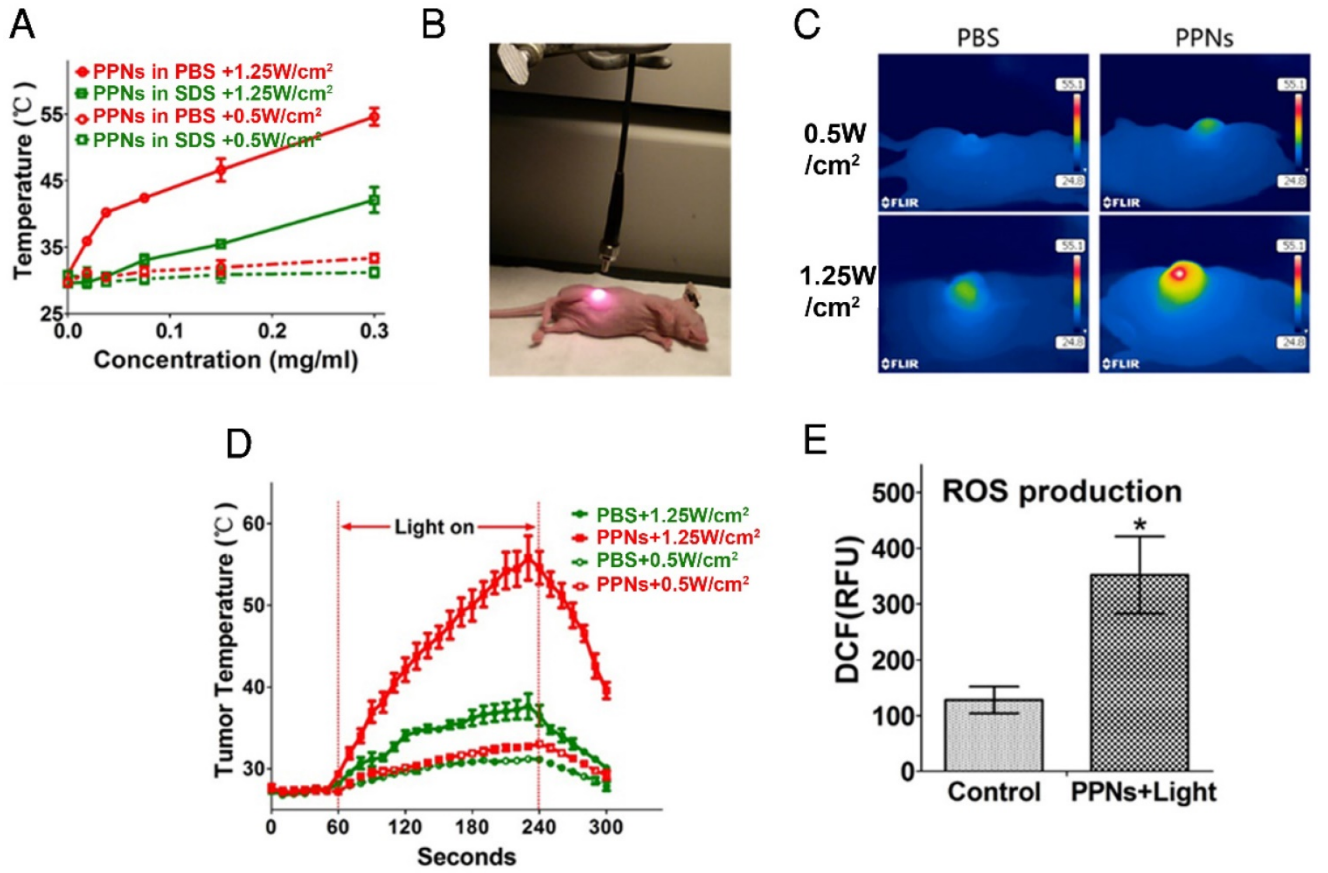

Figure 4. Photothermal transduction of PPNs *in vitro* and *in vivo*. (**A**) Temperature increase curve of PPNs in the absence and in the presence of SDS upon various irradiations with a 690 nm laser at the dose of 0.5W/cm² and 1.25 W/cm² for 30 s (n=3). (**B**) The set-up of the light irradiation showing the position of light source and SKOV-3 tumor-bearing mice. (**C**) Representative thermal images of SKOV-3 tumor-bearing mice 24 hrs after intravenous administration with 2 mg/kg PPNs or PBS. The images were captured by thermal camera in tumors subjected to various irradiations with a 690 nm laser. (**D**) Tumor temperature increase curve during the 180 s laser irradiation (n=3). (**E**) ROS production at the tumor site in SKOV-3 tumor-bearing mice treated with 2 mg/kg PPNs or PBS for 24 hrs followed by various laser irradiations for 2 min (P<0.05).

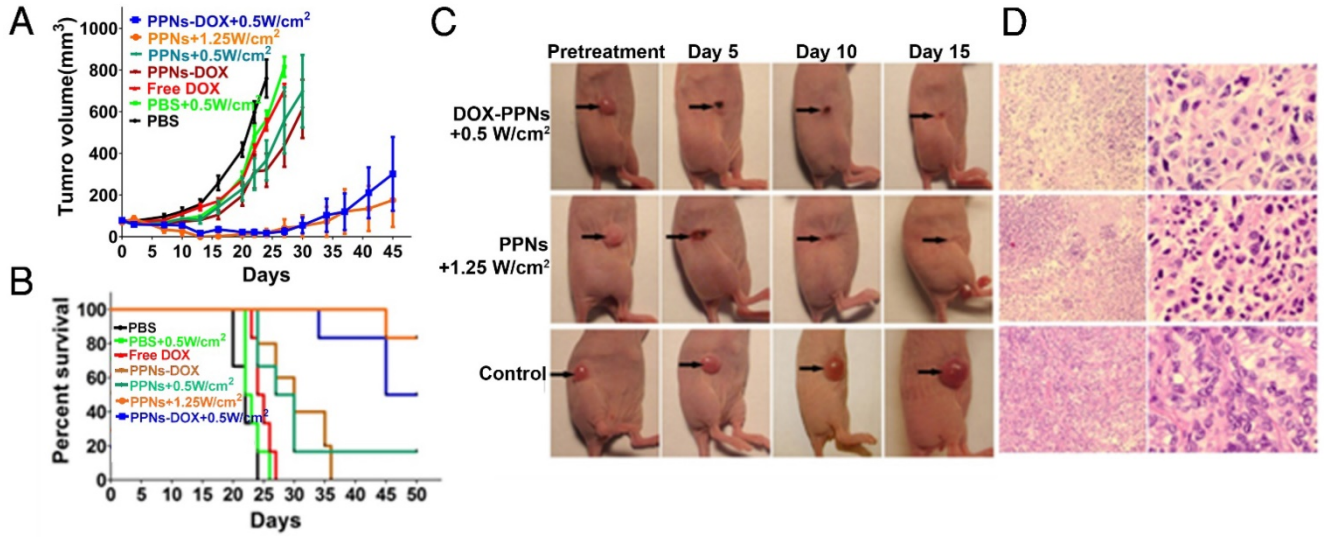

Figure 5. *In vivo* therapeutic response to PPNs mediated chemotherapy combined with photo-therapy. (**A**) *In vivo* antitumor efficacy after the intravenous treatment of various DOX formulations combined with PPNs mediated photo-therapy (n=6). The SKOV-3 tumor-bearing mice were intravenously injected with PBS (control), free DOX (2.5 mg/kg), PPNs (2 mg/kg calculate on porphyrin) and PPNs-DOX (PPNs 2 mg/kg, DOX 2.5 mg/kg) on day 0, 5, 10 and 15 followed by various light irradiations for 2 min on tumors at 24 hrs post injection. (**B**) Kaplan-Meier survival curves of SKOV-3 tumor-bearing mice treated with above indicated conditions (n=6). Tumor volume reached 500 mm³ was considered as the end point of survival data. (**C**) Photographs showing therapeutic response to PPNs mediated phototherapy with irradiation at 0.5 W/cm² for 2 min and 1.25 W/cm² for 2 min, respectively. (**D**) H&E staining of tumor sections collected from control mice and PPNs injected (2 mg/kg) and variously irradiated mice (0.5 W for 2 min and 1.25 W for 2 min, respectively) at 24 hrs post injection.

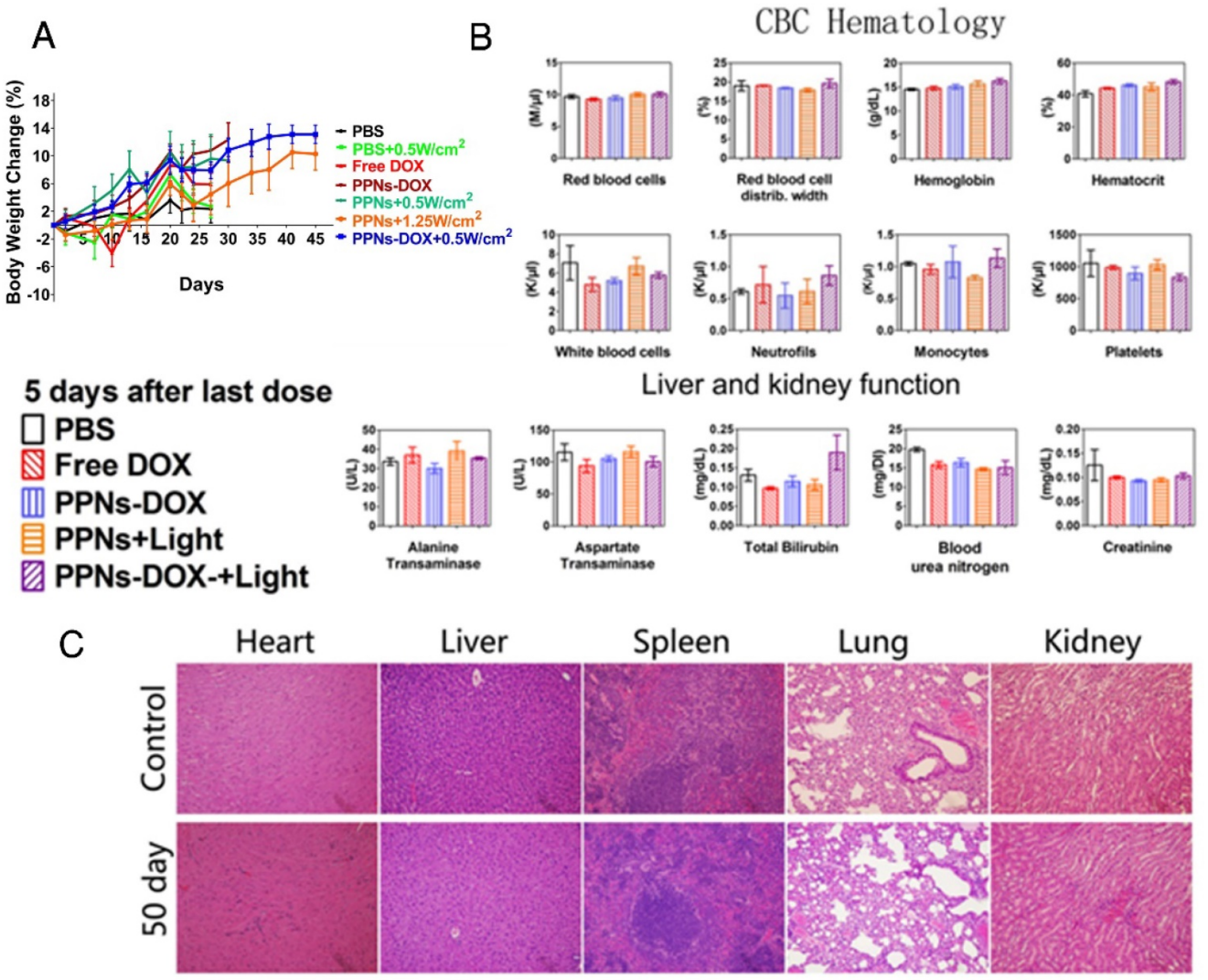

Figure 6. Toxicity analysis of PPNs *in vivo*. (**A**) Body weight changes of SKOV-3 tumor-bearing mice after intravenously treated with various DOX formulations (DOX=2.5 mg/kg, PPNs=2 mg/kg calculate on porphyrin) with or without light irradiation (n=6). (**B**) Blood cell counts and serum chemistry of mice with intravenous administration of PPNs or PBS at day 5 after the last dosage (mean ± SD, n=3). **(C)** Representative H&E stained images of major organs from mice in PBS control group and PPNs-DOX administrated (2 mg/kg, calculated on porphyrin) at day 50 after SKOV-3 injection.

In vivo toxicity evaluation

The potential toxicity of PPNs and the related formulations was assessed in all treated mice. The body weight change, blood cell counts and serum chemistry including renal and hepatic function panels were monitored. Compare to the PBS control group, no obvious body weight loss was observed in all groups (Fig.6A). 5 days after the last dose on day 15, the blood samples were collected for blood cell counts and serum chemistry analysis. As shown in Fig. 6B, red blood cell count, white blood cell count, hemoglobin, platelets and attributes in all treatment groups were very similar to PBS control group after 4 doses of treatment. The renal and hepatic functions of the mice including ALT, AST, BUN and Creatinine were generally within the normal ranges, with the exception of slightly elevated total bilirubin in the combination group after light irradiation was observed (Fig. 6B). After mice in control group and PPNs-DOX group reached the end point on day 50, the major organs were resected for histopathological examination. The results indicated that all the examined organs were in normal condition (Fig.6C).

Discussion

Nanomaterials offer new strategy for cancer therapy by altering pharmacokinetic profile of loaded drugs, reduce systemic toxicity, and improve the therapeutic index [82-84]. However, the use of these clinically approved nanoformulations has not always achieved significantly improved clinical outcomes. Recently, integration of multimodal diagnostic and therapeutic functions within a single nanoparticle has been an attractive research direction in developing next generation of nanoparticles [3, 6-12, 35, 85, 86].

Inorganic nanoparticles have been extensively explored for this application on the basis of their intrinsic capability for photothermal therapy, fluorescence imaging, photoacoustic tomography and magnetic resonance imaging [5, 6, 8, 13, 22, 23]. However, concerns regarding biocompatibility and limited drug loading capacity hindered their further clinical applications. In contrast, organic nanoparticles including liposomes and micelles, have achieved broad clinical implementation due to robust long-term safety and effective drug delivery capacity. However, these carrier-based organic nanoparticles are typically difficult to integrate new therapeutic and imaging modalities. In the present study, by using one single building block, PVA-phorphyrin conjugate and a simple and economic "one-pot" formulation approach, we were able to fabricate a highly versatile and multifunctional PPN nanoplatform in aqueous solutions. The PPNs showed interesting optical properties, with light-absorption and structure dependent fluorescence (self-quenching) in the near-infrared region. In addition to their drug delivery function, PPNs could also be used as photosensitizers for PDT and PTT, as well as imaging probes for NIR fluorescence imaging.

Poly(vinyl alcohol) (PVA), a water-soluble synthetic polymer with simple linear structure, has a well-documented history of biomedical applications, specifically in the form of hydrogel materials and utility in tissue engineering [87, 88]. However, PVA based physical hydrogels failed to appear in the focus of biomedical research due to their hundreds of micrometers in size that largely ruled out nanoscale materials design [89, 90]. Here, we developed PVA-porphyrin conjugates via one step ester formation, which could self-assemble into micellar structure in aqueous solutions, with particle sizes below 100 nm. A variety of hydrophobic drugs and imaging agents could be incorporated during the nanoparticle formation via self-assembly. With well-defined chemical structure, uniform size and narrow size distribution, excellent drug loading efficiency and biocompatibility, the PVA-porphyrin-based nanoparticles offer unprecedented opportunities for bio-imaging and therapeutic applications, including image-guided surgery and intra-operative phototherapy.

PDT and PTT have shown great promise for the treatment of human diseases. In PDT and PTT, photosensitizers are needed for the light energy conversion[56]. So far, most of the PTT agents are based on inorganic nanomaterials [13, 30, 91-96], which demonstrate much larger absorption coefficient in the NIR regions in contrast to the monomeric chromophores. Until recently, a few organic-based nanoparticles, such as photosensitizer-containing micelles, liposomes, and diketopyrrolopyrrole-triphenylamine nanoparticles, were reported to exhibit excellent PTT function [52-56]. In the present study, PPNs were developed to use as an organic dual modal PTT/PDT agent that could be activated by near infrared light at a single excitation wavelength. The PTT effect of PPNs resulted from the unique structure-based highly self-quenching properties of porphyrin, showing comparable photothermal efficiency to inorganic PTT agents. In our animal study, PPNs mediated PTT/PDT was found to be very effective, particularly at high light dose of 1.25 W/cm^2 for 2 min (Figure 5a). At lower light dose of 0.5 W/cm^2 for 2 min, therapeutic effect was only modest, but can be greatly increased by incorporating low dose doxorubicin inside the nanoparticle. This desirable synergistic effect can in part be explained by the non-overlapping mechanisms of PTT/PDT and doxorubicin [97]. The use of important control groups such as "PPNs + light" plus "free Dox" is critical to demonstrate the necessity of making such an all-in-one PPN nanoplatform for fulfilling multitasks concurrently. It will be included in our future study design.

Conclusion

In summary, we have developed a highly versatile and biocompatible theranostic nanoplatform based on PVA-porphyrin assemblies for cancer imaging and therapy through a simple "one-pot" approach. It provides a much easier and cheaper strategy for the integration of multiple imaging and therapeutic modalities towards personalized nanomedicine. The extremely simple production procedure of this type of nanoparticle will greatly facilitate its clinical translation. Our future work will focus on optimizing chemical structures of PPNs, as well as decoration of PPNs with tumor-targeting ligands identified by the well-established "one-bead–one-compound" (OBOC) combinatorial library approach used in our laboratory [98, 99], providing opportunities for further applications against specific cancer type.

Acknowledgements

The authors thank the financial support from NIH/NCI (R01CA199668 & 3R01CA115483), NIH/NIBIB (5R01EB012569), NIH/NICHD (1R01HD086195) and DoD PRMRP Award (W81XWH-13-1-0490).

Supplementary Material

Supplementary figures.
http://www.thno.org/v07p3901s1.pdf

Competing Interests

C. Feng, Y.Li and K.S.L are the inventors of pending patent on PPNs. K.S. L is the founding scientist of LamnoTherapeutics Inc which plan to develop the nanotheranostics described in the manuscript.

References

1. Lu N, Huang P, Fan W, Wang Z, Liu Y, Wang S, et al. Tri-stimuli-responsive biodegradable theranostics for mild hyperthermia enhanced chemotherapy. Biomaterials. 2017; 126: 39-48.
2. Wang Z, Huang P, Jacobson O, Liu Y, Lin L, Lin J, et al. Biomineralization-inspired synthesis of copper sulfide-ferritin nanocages as cancer theranostics. ACS Nano. 2016; 10: 3453-60.
3. Lin J, Wang M, Hu H, Yang X, Wen B, Wang Z, et al. Multimodal-imaging-guided cancer phototherapy by versatile biomimetic theranostics with UV and gamma-irradiation protection. Adv Mater. 2016; 28: 3273-9.
4. Cui H, Wang J. Progress in the development of nanotheranostic systems. Theranostics. 2016; 6: 915-7.
5. Yu J, Yin W, Zheng X, Tian G, Zhang X, Bao T, et al. Smart MoS2/Fe3O4 nanotheranostic for magnetically targeted photothermal therapy guided by magnetic resonance/photoacoustic imaging. Theranostics. 2015; 5: 931-45.
6. Ke H, Wang J, Tong S, Jin Y, Wang S, Qu E, et al. Gold nanoshelled liquid perfluorocarbon magnetic nanocapsules: a nanotheranostic platform for bimodal ultrasound/magnetic resonance imaging guided photothermal tumor ablation. Theranostics. 2013; 4: 12-23.
7. Yang W, Guo W, Le W, Lv G, Zhang F, Shi L, et al. Albumin-bioinspired Gd:CuS nanotheranostic agent for in vivo photoacoustic/magnetic resonance imaging-guided tumor-targeted photothermal therapy. ACS Nano. 2016; 10: 10245-57.
8. Lv G, Guo W, Zhang W, Zhang T, Li S, Chen S, et al. Near-infrared emission CuInS/ZnS quantum dots: all-in-one theranostic nanomedicines with intrinsic fluorescence/photoacoustic imaging for tumor phototherapy. ACS Nano. 2016.
9. Cui L, Lin Q, Jin CS, Jiang W, Huang H, Ding L, et al. A PEGylation-free biomimetic porphyrin nanoplatform for personalized cancer theranostics. ACS Nano. 2015; 9: 4484-95.
10. Chen Q, Wang X, Wang C, Feng L, Li Y, Liu Z. Drug-induced self-assembly of modified albumins as nano-theranostics for tumor-targeted combination therapy. ACS Nano. 2015; 9: 5223-33.
11. Jain S, Doshi AS, Iyer AK, Amiji MM. Multifunctional nanoparticles for targeting cancer and inflammatory diseases. J Drug Target. 2013; 21:888-903.
12. Zhang L, Dong WF, Sun HB. Multifunctional superparamagnetic iron oxide nanoparticles: design, synthesis and biomedical photonic applications. Nanoscale. 2013; 5: 7664-84.
13. Chen F, Hong H, Goel S, Graves SA, Orbay H, Ehlerding EB, et al. In vivo tumor vasculature targeting of CuS@MSN based theranostic nanomedicine. ACS Nano. 2015; 9: 3926-34.
14. Chen YP, Lv JW, Liu X, Zhang Y, Guo Y, Lin AH, et al. The landscape of clinical trials evaluating the theranostic role of PET imaging in oncology: insights from an analysis of clinicaltrials. Theranostics. 2017; 7: 390-9.
15. Hung CC, Huang WC, Lin YW, Yu TW, Chen HH, Lin SC, et al. Active tumor permeation and uptake of surface charge-switchable theranostic nanoparticles for imaging-guided photothermal/chemo combinatorial therapy. Theranostics. 2017; 7: 559-60.
16. Martinho O, Silva-Oliveira R, Cury FP, Barbosa AM, Granja S, Evangelista AF, et al. HER family receptors are important theranostic biomarkers for cervical cancer: blocking glucose metabolism enhances the therapeutic effect of HER inhibitors. Theranostics. 2017; 7: 717-32.
17. Su J, Sun H, Meng Q, Zhang P, Yin Q, Li Y. Enhanced blood suspensibility and laser-activated tumor-specific drug release of theranostic mesoporous silica nanoparticles by functionalizing with erythrocyte membranes. Theranostics. 2017; 7: 523-37.
18. Xiaowei Ma YZ, and Xing-Jie Liang. Theranostic nanoparticles engineered for clinic and pharmaceutics. Acc Chem Res. 2011; 44: 1114-22.
19. Cheng Q, Sui J, Li Y, Zhou Z, Cai W. Facile synthesis of multifunctional beta-NaGdF4:Yb3+/Er3+ nanoparticles in oleylamine. J Nanosci Nanotechnol. 2013; 13: 529-32.
20. Hu X, Hao X, Wu Y, Zhang J, Zhang X, Wang PC, et al. Multifunctional hybrid silica nanoparticles for controlled doxorubicin loading and release with thermal and pH dually response. J Mater Chem B Mater Biol Med. 2013; 1: 1109-18.
21. Wang Q, Zhuang X, Mu J, Deng ZB, Jiang H, Xiang X, et al. Delivery of therapeutic agents by nanoparticles made of grapefruit-derived lipids. Nat Commun. 2013; 4: 1867.
22. Qi L, Gao X. Emerging application of quantum dots for drug delivery and therapy. Expert Opin Drug Deliv. 2008; 5: 263-7.
23. Mahmoudi M, Sant S, Wang B, Laurent S, Sen T. Superparamagnetic iron oxide nanoparticles (SPIONs): development, surface modification and applications in chemotherapy. Adv. Drug Deliv. Rev. 2011; 63: 24-46.
24. Laurent S, Forge D, Port M, Roch A, Robic C, Vander Elst L, et al. Magnetic iron oxide nanoparticles: synthesis, stabilization, vectorization, physicochemical characterizations, and biological applications. Chem Rev. 2008; 108: 2064-110.
25. Lee GY, Qian WP, Wang L, Wang YA, Staley CA, Satpathy M, et al. Theranostic nanoparticles with controlled release of gemcitabine for targeted therapy and MRI of pancreatic cancer. ACS Nano. 2013; 7: 2078-89.
26. Wang C, Xu H, Liang C, Liu Y, Li Z, Yang G, et al. Iron oxide @ polypyrrole nanoparticles as a multifunctional drug carrier for remotely controlled cancer therapy with synergistic antitumor effect. ACS Nano. 2013; 7: 6782-95.
27. Chen J, Glaus C, Laforest R, Zhang Q, Yang M, Gidding M, et al. Gold nanocages as photothermal transducers for cancer treatment. Small. 2010; 6: 811-7.
28. Wang Y, Black KC, Luehmann H, Li W, Zhang Y, Cai X, et al. Comparison study of gold nanohexapods, nanorods, and nanocages for photothermal cancer treatment. ACS Nano. 2013; 7: 2068-77.
29. Jing L, Liang X, Li X, Lin L, Yang Y, Yue X, et al. Mn-porphyrin conjugated Au nanoshells encapsulating doxorubicin for potential magnetic resonance imaging and light triggered synergistic therapy of cancer. Theranostics. 2014; 4: 858-71.
30. Zhang Z, Wang L, Wang J, Jiang X, Li X, Hu Z, et al. Mesoporous silica-coated gold nanorods as a light-mediated multifunctional theranostic platform for cancer treatment. Adv Mater. 2012; 24: 1418-23.
31. Schwartzberg AM, Olson TY, Talley CE, Zhang JZ. Synthesis, characterization, and tunable optical properties of hollow gold nanospheres. J Phys Chem B. 2006; 110: 19935-44.
32. You J, Zhang G, Li C. Exceptionally high payload of doxorubicin in hollow gold nanospheres for near-infrared light-triggered drug release. ACS Nano. 2010; 4: 1033-41.
33. Bhirde AA, Chikkaveeraiah BV, Srivatsan A, Niu G, Jin AJ, Kapoor A, et al. Targeted therapeutic nanotubes influence the viscoelasticity of cancer cells to overcome drug resistance. ACS Nano. 2014; 8: 4177-89.
34. Yang K, Zhang S, Zhang G, Sun X, Lee ST, Liu Z. Graphene in mice: ultrahigh in vivo tumor uptake and efficient photothermal therapy. Nano Lett. 2010; 10: 3318-23.
35. Zhao Z, Zhou Z, Bao J, Wang Z, Hu J, Chi X, et al. Octapod iron oxide nanoparticles as high-performance T2 contrast agents for magnetic resonance imaging. Nat Commun. 2013; 4: 2266.
36. Zhang R, Zhang Y, Zhang Q, Xie H, Wang H, Nie J, et al. Optical visualization of individual ultralong carbon nanotubes by chemical vapour deposition of titanium dioxide nanoparticles. Nat Commun. 2013; 4: 1727.
37. Swierczewska M, Lee S, Chen X. Inorganic nanoparticles for multimodal molecular imaging. Mol Imaging. 2011; 10: 3-16.
38. Lewinski N, Colvin V, Drezek R. Cytotoxicity of nanoparticles. Small. 2008; 4: 26-49.
39. Li R, Wang X, Ji Z, Sun B, Zhang H, Chang CH, et al. Surface charge and cellular processing of covalently functionalized multiwall carbon nanotubes determine pulmonary toxicity. ACS Nano. 2013; 7: 2352-68.
40. Nel A, Xia T, Meng H, Wang X, Lin S, Ji Z, et al. Nanomaterial toxicity testing in the 21st century: use of a predictive toxicological approach and high-throughput screening. Acc Chem Res. 2013; 46: 607-21.
41. George S, Lin S, Ji Z, Thomas CR, Li L, Mecklenburg M, et al. Surface defects on plate-shaped silver nanoparticles contribute to its hazard potential in a fish gill cell line and zebrafish embryos. ACS Nano. 2012; 6: 3745-59.
42. Gilbert B, Fakra SC, Xia T, Pokhrel S, Madler L, Nel AE. The fate of ZnO nanoparticles administered to human bronchial epithelial cells. ACS Nano. 2012; 6: 4921-30.
43. Markus Antonietti SF. Vesicles and liposomes: a self-assembly principle beyond lipids. Adv Mater. 2003; 15: 1323-33.
44. Xiao K, Luo J, Li Y, Lee JS, Fung G, Lam KS. PEG-oligocholic acid telodendrimer micelles for the targeted delivery of doxorubicin to B-cell lymphoma. J Control Release. 2011; 155: 272-81.
45. Luo J, Xiao K, Li Y, Lee JS, Shi L, Tan YH, et al. Well-defined, size-tunable, multifunctional micelles for efficient paclitaxel delivery for cancer treatment. Bioconjug Chem. 2010; 21: 1216-24.
46. Kato J, Li Y, Xiao K, Lee JS, Luo J, Tuscano JM, et al. Disulfide cross-linked micelles for the targeted delivery of vincristine to B-cell lymphoma. Mol Pharm. 2012; 9: 1727-35.
47. Li Y, Lin TY, Luo Y, Liu Q, Xiao W, Guo W, et al. A smart and versatile theranostic nanomedicine platform based on nanoporphyrin. Nat commun. 2014; 5: 4712.
48. Davis ME, Chen ZG, Shin DM. Nanoparticle therapeutics: an emerging treatment modality for cancer. Nat Rev Drug Discov. 2008; 7: 771-82.
49. Kim BY, Rutka JT, Chan WC. Nanomedicine. New Eng J Med. 2010; 363: 2434-43.
50. Hrkach J, Von Hoff D, Mukkaram Ali M, Andrianova E, Auer J, Campbell T, et al. Preclinical development and clinical translation of a PSMA-targeted docetaxel nanoparticle with a differentiated pharmacological profile. Sci. Transl. Med. 2012; 4: 128ra39.
51. Lovell JF, Jin CS, Huynh E, Jin H, Kim C, Rubinstein JL, et al. Porphysome nanovesicles generated by porphyrin bilayers for use as multimodal biophotonic contrast agents. Nat Mater. 2011; 10: 324-32.

52. Huang Y, Qiu F, Shen L, Chen D, Su Y, Yang C, et al. Combining two-photon-activated fluorescence resonance energy transfer and near-Infrared photothermal effect of unimolecular micelles for enhanced photodynamic therapy. ACS Nano. 2016; 10: 10489-99.
53. Wang K, Zhang Y, Wang J, Yuan A, Sun M, Wu J, et al. Self-assembled IR780-loaded transferrin nanoparticles as an imaging, targeting and PDT/PTT agent for cancer therapy. Sci. Rep. 2016; 6: 27421.
54. Yan F, Wu H, Liu H, Deng Z, Duan W, Liu X, et al. Molecular imaging-guided photothermal/photodynamic therapy against tumor by iRGD-modified indocyanine green nanoparticles. J Control Release. 2016; 224: 217-28.
55. Li W, Peng J, Tan L, Wu J, Shi K, Qu Y, et al. Mild photothermal therapy/photodynamic therapy/chemotherapy of breast cancer by Lyp-1 modified Docetaxel/IR820 Co-loaded micelles. Biomaterials. 2016; 106: 119-33.
56. Cai Y, Liang P, Tang Q, Yang X, Si W, Huang W, et al. Diketopyrrolopyrrole-triphenylamine organic nanoparticles as multifunctional reagents for photoacoustic imaging-guided photodynamic/photothermal synergistic tumor therapy. ACS Nano. 2017; 11: 1054-63.
57. Press AT, Traeger A, Pietsch C, Mosig A, Wagner M, Clemens MG, et al. Cell type-specific delivery of short interfering RNAs by dye-functionalised theranostic nanoparticles. Nat Commun. 2014; 5: 5565.
58. Cheng L, Yang K, Chen Q, Liu Z. Organic stealth nanoparticles for highly effective in vivo near-infrared photothermal therapy of cancer. ACS Nano. 2012; 6: 5605-13.
59. Smith BR, Gambhir SS. Nanomaterials for In Vivo Imaging. Chemical reviews. 2017; 117: 901-86.
60. Svenson S. The dendrimer paradox - high medical expectations but poor clinical translation. Chem Soc Rev. 2015; 44: 4131-44.
61. Wicki A, Witzigmann D, Balasubramanian V, Huwyler J. Nanomedicine in cancer therapy: Challenges, opportunities, and clinical applications. J Control Release. 2015; 200: 138-57.
62. Mahajan A, Goh V, Basu S, Vaish R, Weeks AJ, Thakur MH, et al. Bench to bedside molecular functional imaging in translational cancer medicine: to image or to imagine? Clin Radiol. 2015; 70: 1060-82.
63. Mandal B, Bhattacharjee H, Mittal N, Sah H, Balabathula P, Thoma LA, et al. Core-shell-type lipid-polymer hybrid nanoparticles as a drug delivery platform. Nanomedicine: NBM. 2013; 9: 474-91.
64. Cheng L, Wang C, Feng LZ, Yang K, Liu Z. Functional Nanomaterials for Phototherapies of Cancer. Chem Rev. 2014; 114: 10869-939.
65. Luo DD, Carter KA, Miranda D, Lovell JF. Chemophototherapy: An Emerging Treatment Option for Solid Tumors. Adv Sci. 2017; 4.
66. Agarwal A, Mackey MA, El-Sayed MA, Bellamkonda RV. Remote Triggered Release of Doxorubicin in Tumors by Synergistic Application of Thermosensitive Liposomes and Gold Nanorods. ACS Nano. 2011; 5: 4919-26.
67. Luo DD, Carter KA, Razi A, Geng JM, Shao S, Giraldo D, et al. Doxorubicin encapsulated in stealth liposomes conferred with light-triggered drug release. Biomaterials. 2016; 75: 193-202.
68. Lovell JF, Jin CS, Huynh E, Jin H, Kim C, Rubinstein JL, et al. Porphysome nanovesicles generated by porphyrin bilayers for use as multimodal biophotonic contrast agents. Nat Mater. 2011; 10: 324-32.
69. Shahbazi-Gahrouei D WM, Allen BJ. Synthesis and application of new gadolinium-porphyrins as poterntial. MR imaging contrast agents for cancer detection in nude mice. Iran Biomed J. 2001; 5: 87-95.
70. Qin SP, Seo JW, Zhang H, Qi J, Curry FRE, Ferrara KW. An imaging-driven model for liposomal stability and circulation. Mol Pharmaceut. 2010; 7: 12-21.
71. Rygh CB, Qin SP, Seo JW, Mahakian LM, Zhang H, Adamson R, et al. Longitudinal investigation of permeability and distribution of macromolecules in mouse malignant transformation using PET. Clin Cancer Res. 2011; 17: 550-9.
72. Seo JW, Qin SP, Mahakian LM, Watson KD, Kheirolomoom A, Ferrara KW. Positron emission tomography imaging of the stability of Cu-64 labeled dipalmitoyl and distearoyl lipids in liposomes. J Control Release. 2011; 151: 28-34.
73. Watson KD, Lai CY, Qin S, Kruse DE, Lin YC, Seo JW, et al. Ultrasound increases nanoparticle delivery by reducing intratumoral pressure and increasing transport in epithelial and epithelial-mesenchymal transition tumors. Cancer Res. 2012; 72: 1485-93.
74. Denardo SJ, Liu R, Albrecht H, Natarajan A, Sutcliffe JL, Anderson C, et al. 111In-LLP2A-DOTA polyethylene glycol-targeting (alpha)4(beta)1 integrin: comparative pharmacokinetics for imaging and therapy of lymphoid malignancies. J Nucl Med. 2009; 50: 625-34.
75. Chen K, Preuss A, Hackbarth S, Wacker M, Langer K, Roder B. Novel photosensitizer-protein nanoparticles for photodynamic therapy: photophysical characterization and in vitro investigations. J Photochem Photobiol. 2009; 96: 66-74.
76. Li MQ, Tang ZH, Lv SX, Song WT, Hong H, Jing XB, et al. Cisplatin crosslinked pH-sensitive nanoparticles for efficient delivery. of doxorubicin. Biomaterials. 2014; 35: 3851-64.
77. Nasongkla N, Bey E, Ren JM, Ai H, Khemtong C, Guthi JS, et al. Multifunctional polymeric micelles as cancer-targeted, MRI-ultrasensitive drug delivery systems. Nano Lett. 2006; 6: 2427-30.
78. Lefrak EA, Pi ha J., Rosenheim S and Gottlieb JA. A clinicopathologic analysis of adriamycin cardiotoxicity. Cancer. 1973; 32: 302-14.
79. Bases R, et al. Attempts at tumor localization using CU64-labeled copper porphyrins. Cancer. 1958; 11: 259-63.
80. Shahbazi-Gahrouei D. Gadolinium-porphyrins: new potential magnetic resonance imaging contrast agents for melanoma detection. J Res Med Sci. 2006; 11: 217-23.
81. Jiyun Shi TWBL, Juan Chen, David Green, David Jaffray, Brian C. Wilson, Fan Wang and Gang Zheng. Transforming a targeted porphyrin theranostic agent into a PET imaging probe for cancer. Theranostics. 2011; 1: 363-70.
82. Nair M, Guduru R, Liang P, Hong J, Sagar V, Khizroev S. Externally controlled on-demand release of anti-HIV drug using magneto-electric nanoparticles as carriers. Nat Commun. 2013; 4: 1707.
83. Soppimath KS, Aminabhavi TM, Kulkarni AR, Rudzinski WE. Biodegradable polymeric nanoparticles as drug delivery devices. J Control Release. 2001; 70: 1-20.
84. Meng H, Mai WX, Zhang H, Xue M, Xia T, Lin S, et al. Codelivery of an optimal drug/siRNA combination using mesoporous silica nanoparticles to overcome drug resistance in breast cancer in vitro and in vivo. ACS Nano. 2013; 7: 994-1005.
85. Xiong B, Zhou R, Hao J, Jia Y, He Y, Yeung ES. Highly sensitive sulphide mapping in live cells by kinetic spectral analysis of single Au-Ag core-shell nanoparticles. Nat Commun. 2013; 4: 1708.
86. Tan WB, Jiang S, Zhang Y. Quantum-dot based nanoparticles for targeted silencing of HER2/neu gene via RNA interference. Biomaterials. 2007; 28: 1565-71.
87. Hassan CM, Stewart JE, Peppas NA. Diffusional characteristics of freeze/thawed poly(vinyl alcohol) hydrogels: applications to protein controlled release from multilaminate devices. Eur J Pharm Biopharm. 2000; 49: 161-5.
88. Lozinsky VI, Galaev IY, Plieva FM, Savina IN, Jungvid H, Mattiasson B. Polymeric cryogels as promising materials of biotechnological interest. Trends Biotechnol. 2003; 21: 445-51.
89. Plieva FM, Galaev IY, Mattiasson B. Macroporous gels prepared at subzero temperatures as novel materials for chromatography of particulate-containing fluids and cell culture applications. J Sep Sci. 2007; 30: 1657-71.
90. Jensen BE, Smith AA, Fejerskov B, Postma A, Senn P, Reimhult E, et al. Poly(vinyl alcohol) physical hydrogels: noncryogenic stabilization allows nano- and microscale materials design. Langmuir. 2011; 27: 10216-23.
91. Rossella F, Soldano C, Bellani V, Tommasini M. Metal-filled carbon nanotubes as a novel class of photothermal nanomaterials. Adv Mater. 2012; 24: 2453-8.
92. Antaris AL, Robinson JT, Yaghi OK, Hong G, Diao S, Luong R, et al. Ultra-low doses of chirality sorted (6,5) carbon nanotubes for simultaneous tumor imaging and photothermal therapy. ACS Nano. 2013; 7: 3644-52.
93. Guo Y, Zhang Z, Kim DH, Li W, Nicolai J, Procissi D, et al. Photothermal ablation of pancreatic cancer cells with hybrid iron-oxide core gold-shell nanoparticles. Int J Nanomed. 2013; 8: 3437-46.
94. Lin J, Wang S, Huang P, Wang Z, Chen S, Niu G, et al. Photosensitizer-loaded gold vesicles with strong plasmonic coupling effect for imaging-guided photothermal/photodynamic therapy. ACS Nano. 2013; 7: 5320-9.
95. Song J, Yang X, Jacobson O, Lin L, Huang P, Niu G, et al. Sequential drug release and enhanced photothermal and photoacoustic effect of hybrid reduced graphene oxide-loaded ultrasmall gold nanorod vesicles for cancer therapy. ACS Nano. 2015; 9: 9199-209.
96. Zhang L, Su H, Cai J, Cheng D, Ma Y, Zhang J, et al. A multifunctional platform for tumor angiogenesis-targeted chemo-thermal therapy using polydopamine-coated gold nanorods. ACS Nano. 2016; 10: 10404-17.
97. Creekmore SP, Zaharko DS. Modification of chemotherapeutic effects on L1210 cells using hematoporphyrin and light. Cancer Res. 1983; 43: 5252-7.
98. Lam KS, Salmon SE, Hersh EM, Hruby VJ, Kazmierski WM, Knapp RJ. A new type of synthetic peptide library for identifying ligand-binding activity. Nature. 1991; 354: 82-4.
99. Xiao W, Bononi FC, Townsend J, Li Y, Liu R, Lam KS. Immobilized OBOC combinatorial bead array to facilitate multiplicative screening. Comb Chem High Throughput Screen. 2013; 16: 441-8.